

# Tracing immune cells around biomaterials with spatial anchors during large-scale wound regeneration

Received: 20 October 2022

Accepted: 11 September 2023

Published online: 26 September 2023

 Check for updatesYang Yang<sup>1,2,3</sup>, Chenyu Chu<sup>1,3</sup>, Li Liu<sup>1,3</sup>, Chenbing Wang<sup>1</sup>, Chen Hu<sup>1</sup>, Shengan Rung<sup>1,2</sup>, Yi Man<sup>1,4</sup>✉ & Yili Qu<sup>2,4</sup>✉

Skin scarring devoid of dermal appendages after severe trauma has unfavorable effects on aesthetic and physiological functions. Here we present a method for large-area wound regeneration using biodegradable aligned extracellular matrix scaffolds. We show that the implantation of these scaffolds accelerates wound coverage and enhances hair follicle neogenesis. We perform multimodal analysis, in combination with single-cell RNA sequencing and spatial transcriptomics, to explore the immune responses around biomaterials, highlighting the potential role of regulatory T cells in mitigating tissue fibrosis by suppressing excessive type 2 inflammation. We find that immunodeficient mice lacking mature T lymphocytes show the typical characteristic of tissue fibrosis driven by type 2 macrophage inflammation, validating the potential therapeutic effect of the adaptive immune system activated by biomaterials. These findings contribute to our understanding of the coordination of immune systems in wound regeneration and facilitate the design of immunoregulatory biomaterials in the future.

After severe skin damage, the resulting scar usually contains dense extracellular matrix (ECM) fibers devoid of the hair follicle (HF) and sebaceous gland (SG), which lack sensation and endocrine function as well as the flexibility of normal skin<sup>1</sup>. As a result, there is an urgent need to explore the fundamental mechanisms stimulating HF regeneration in skin repair. The immune system plays a varying role in driving scar fibrosis<sup>2–4</sup> or HF regeneration<sup>5–8</sup> upon different environmental stimuli. Macrophages contribute to all phases of tissue repair, and the heterogeneity of macrophages is believed to be one of the critical orchestrators determining the healing outcome<sup>9,10</sup>. Two major subpopulations, including pro-inflammatory M1-like and anti-inflammatory M2-like, have been credited with these distinct roles<sup>11</sup>. It has been reported that the pro-inflammatory macrophage-elicited pro-inflammatory mediators, such as tumor necrosis factor (TNF)<sup>5</sup> and interleukin-1 beta (IL-1 $\beta$ )<sup>12</sup>, effectively promote subsequent HF

neogenesis. In contrast, type-2 anti-inflammatory macrophages might play an essential role in wound fibrosis by promoting fibrotic fibroblast activation and collagen cross-linking<sup>3</sup> via fibrotic cytokines such as transforming growth factor- $\beta$  (TGF- $\beta$ )<sup>13</sup> and RELM $\alpha$ <sup>14</sup> or chronic phagocytosis activity<sup>4</sup> at a later stage. Although the role of macrophages in pathogen clearance and tissue fibrosis<sup>15</sup> has long been stressed, only recently have the T lymphocytes been more thoroughly investigated. In addition to  $\gamma\delta$  T cells that induce HF neogenesis through the secretion of fibroblast growth factor 9 (Fgf9)<sup>6</sup>, the adaptive T cells are being explored to gain more understanding of its role in regulating macrophage polarization and, thus, wound regeneration<sup>2</sup>. T cells coordinate the polarized immune responses through differentiation into specialized subsets of helper T cells (Th1, Th2, and Th17) and drive the type 1/2/3 paradigm of immunity<sup>16</sup>. Besides, specialized regulatory T cells (Tregs) have evolved to counterbalance the

<sup>1</sup>Department of Oral Implantology & State Key Laboratory of Oral Diseases and National Clinical Research Center for Oral Diseases, West China Hospital of Stomatology, Sichuan University, Chengdu 610041, China. <sup>2</sup>Department of Prosthodontics & State Key Laboratory of Oral Diseases and National Clinical Research Center for Oral Diseases, West China Hospital of Stomatology, Sichuan University, Chengdu 610041, China. <sup>3</sup>These authors contributed equally: Yang Yang, Chenyu Chu, Li Liu. <sup>4</sup>These authors jointly supervised this work: Yi Man, Yili Qu. ✉e-mail: [manyi780203@126.com](mailto:manyi780203@126.com); [qqyili@126.com](mailto:qqyili@126.com)

potentially detrimental effect of the innate immune system by suppressing macrophage response<sup>17</sup> and facilitating wound regeneration.

Recently, tissue regeneration mediated by immunoregulatory biomaterials are emerging as a prospective strategy in tissue engineering<sup>18,19</sup>. Biological cues can be integrated into a polymer scaffold to mimic the native ECM, which guides tissue regeneration<sup>20,21</sup>. Upon materials implantation, the foreign body responses (FBR) process initiates with an immune response. It has been shown that modulating FBR by adjusting biomaterials characteristics may create a desired biological response to mobilize stem cells or stimulate specific cell proliferation<sup>20,21</sup>. Our previous studies had reported the Aligned nanofibers scaffold with an immunomodulatory effect in accelerating small skin wound (diameter = 6 mm) re-epithelialization<sup>22,23</sup>. However, scar tissue induced by a 6-mm-scale wound was tiny (diameter = 1–1.5 mm). Considering the more obvious inflammatory response and larger detectable scar tissue, the large-scale full-thickness wound model (diameter = 10–20 mm)<sup>24–28</sup> provided a better media through which we can easily evaluate the pro-regenerative effect of ECM scaffolds regarding scarless wound healing.

Currently, high-resolution techniques such as single-cell RNA sequencing (scRNA-seq)<sup>22,29,30</sup> have been applied to identify rare cell subpopulations in the implantation model but lack information on spatial distribution. Development in spatial transcriptomics (ST) has enabled the assessment of gene expression at spatial resolution<sup>31</sup>, which has been applied to the study of cancer<sup>32,33</sup>, liver<sup>34</sup>, and brain tissue<sup>35</sup> to detect regional cellular communication. The wound healing model with implanted biomaterials provides an ideal method to understand the FBR and probe the role of the immune system in tissue regeneration. To our knowledge, multi-omic approaches, including scRNA-seq and ST, were first applied to trace spatial heterogeneity in the biomaterial-mediated skin wound healing process in this study.

Here, we unveil the cell composition around the ECM scaffold in both wildtype and immunodeficient mice to anchor the critical role of T cells in HF regeneration, which would help optimize the existing biomaterial constructs and provide feasible strategies for the design of novel immunoregulatory products in tissue engineering for biomedical use.

## Results

### Enhanced HF neogenesis in scaffold-implanted wounds with activation of the adaptive immune system

The workflow for evaluating large wound healing is summarized in Fig. 1a. We placed ECM scaffolds below the large wound (diameter = 1.5 cm) in the ECM\_LW (Large wound treated with ECM scaffold) group, while the Ctrl\_LW (Large wound treated with saline) group received no biomaterials (Fig. 1b). C57BL/6 mice are a classical choice for studying wound healing due to their accessibility, affordability, and ease of handling. It is worth noting that wound healing in rodent models primarily relies on contraction by the panniculus carnosus for wound closure, whereas in humans, re-epithelialization and granulation tissue formation play a larger role<sup>36</sup>. As shown in Supplementary Fig. 1a, we created a splinted wound excisional model that could restrict the contraction of the panniculus carnosus, while the unsplit group was treated without a silicone splint. The decreased rate of wound closure (Supplementary Fig. 1b) and the increased granulation formation and de novo HFs were observed in the splinted mice (Supplementary Fig. 1c–e). In order to minimize wound contraction in rodents and mimic the wound-healing process in humans with tight skin, we chose the splinted wound-healing model for further evaluation. Wound coverage was faster in the ECM\_LW group on postoperative day (POD) 7 (Fig. 1c, d), and the ECM\_LW group also had a smaller epithelial gap width on POD 7 and POD 14 (Fig. 1e, f). Immunofluorescence (IF) staining for cytokeratin 5 (KRT5) and cytokeratin 10 (KRT10) showed that keratinocytes crawled around the biomaterials,

and the ECM\_LW group owned a larger area of neo-epithelium (Supplementary Fig. 2a).

In the Ctrl\_LW group, there was limited HF neogenesis restricted in the wound center since the POD 21. In comparison, we observed that the ECM\_LW group recapitulated the normal skin architecture with an equivalent number of mature HF (Fig. 1e, h, Supplementary Fig. 1e). The nascent HFs induced by ECM scaffolds mimicked embryonic hair follicle development pattern (Fig. 1e, g), with high KRT17 (green) in hair germ (HG) and TWIST2 (red) in dermal condensate (Dc) on POD7. After morphogenesis, neogenic HFs in the ECM\_LW group contained proliferating epithelial cells expressing Ki67 (red) with sebaceous glands (SCDI/ green). Of note, the ECM membrane implanted in the large wound did not trigger any obvious fibrous capsule and exhibited an appropriate degradation rate in vivo. We observed degrading fragments on POD14, and no visible particles remained on POD28 (Fig. 1e). The excellent biocompatibility and degradability of the membrane could prevent the risk of immune rejection and secondary surgery in further clinical applications.

To explore the underlying mechanism, a bulk-tissue RNA-seq (bulk-seq) analysis was conducted for two groups harvested on POD 7 ( $n = 3$  for each group). Gene enrichment analysis of Ctrl\_LW group up-regulated genes ( $p$  value  $< 0.05$  and  $|\log_2\text{FoldChange}| > 1$ ) illustrated a state readied to incite innate immune responses (Fig. 1i and Supplementary Fig. 2b), indicated by neutrophil chemotaxis and macrophage activation via type 2 immune response. It has been reported that type 2 cytokines such as interleukin 4 receptor, alpha (IL-4R $\alpha$ ) could activate anti-inflammatory macrophages and lead to the cross-linking of collagen fibers in scar formation<sup>3</sup>. The accumulation of type 2 myeloid immune cells in the Ctrl\_LW group might be the reason for excessive extracellular matrix organization. In contrast, enrichment analysis of ECM up-regulated genes ( $p$  value  $< 0.05$  and  $|\log_2\text{FoldChange}| > 1$ ) revealed enrichment of hair follicle development and mesenchyme morphogenesis driven by Wnt signaling pathway and Hedgehog signaling pathway in the ECM\_LW group (Fig. 1i and Supplementary Fig. 2c). The role of Wnt and Hedgehog signaling pathway in regulating T cell development<sup>37–39</sup> as well as hair follicle regeneration<sup>40,41</sup> had been stressed. We noticed that genes such as frizzled class receptor 5 (*Fzd5*), GATA binding protein 3 (*Gata3*), and GLI family zinc finger 3 (*Gli3*) also enriched in T cell differentiation in the thymus. Besides, *Gata3* expressed by regulatory T cells (Tregs) are proven to be necessary to prevent excessive collagen deposition driven by type-2 macrophage inflammation<sup>42</sup>, which implicated the importance of adaptive immune system homeostasis in material-primed skin regeneration. Flow cytometry (Fig. 1j and Supplementary Fig. 3) and immunohistochemistry (IHC) staining (Supplementary Fig. 2d) confirmed the increased T cell (CD3<sup>+</sup>) infiltration around implanted biomaterials in the early phase.

### A single-cell atlas of the biomaterials tissue microenvironment

To explore the spatial characteristics of single cells during wound healing, we applied ST and scRNA-seq to compare the spatial gene expression profiles between two groups (Fig. 2a). At first, to explore the cell composition in the biomaterial-treated wound, we isolated cells from the ECM\_LW and Ctrl\_LW samples on POD 7, 14, and 21, and applied them to the 10x scRNA-seq platform (Supplementary Fig. 4a). After cell filtering, unsupervised clustering of Seurat categorized the cells into clusters based on global gene expression patterns. Later, clusters were then assigned to first-level main classes of cells. The composition of each main cluster was listed so that the proportion of cells from two groups could be identified across all cell clusters (Supplementary Fig. 4b). Marker genes for each main cluster were shown in the heatmap and listed in Supplementary Fig. 4c. Volcano plot showed genes related to the innate immune system were up-regulated in the Ctrl\_LW group (Supplementary Fig. 4d).

Firstly, we selected main clusters defined as keratinocytes and subjected them to a second round of unsupervised clustering

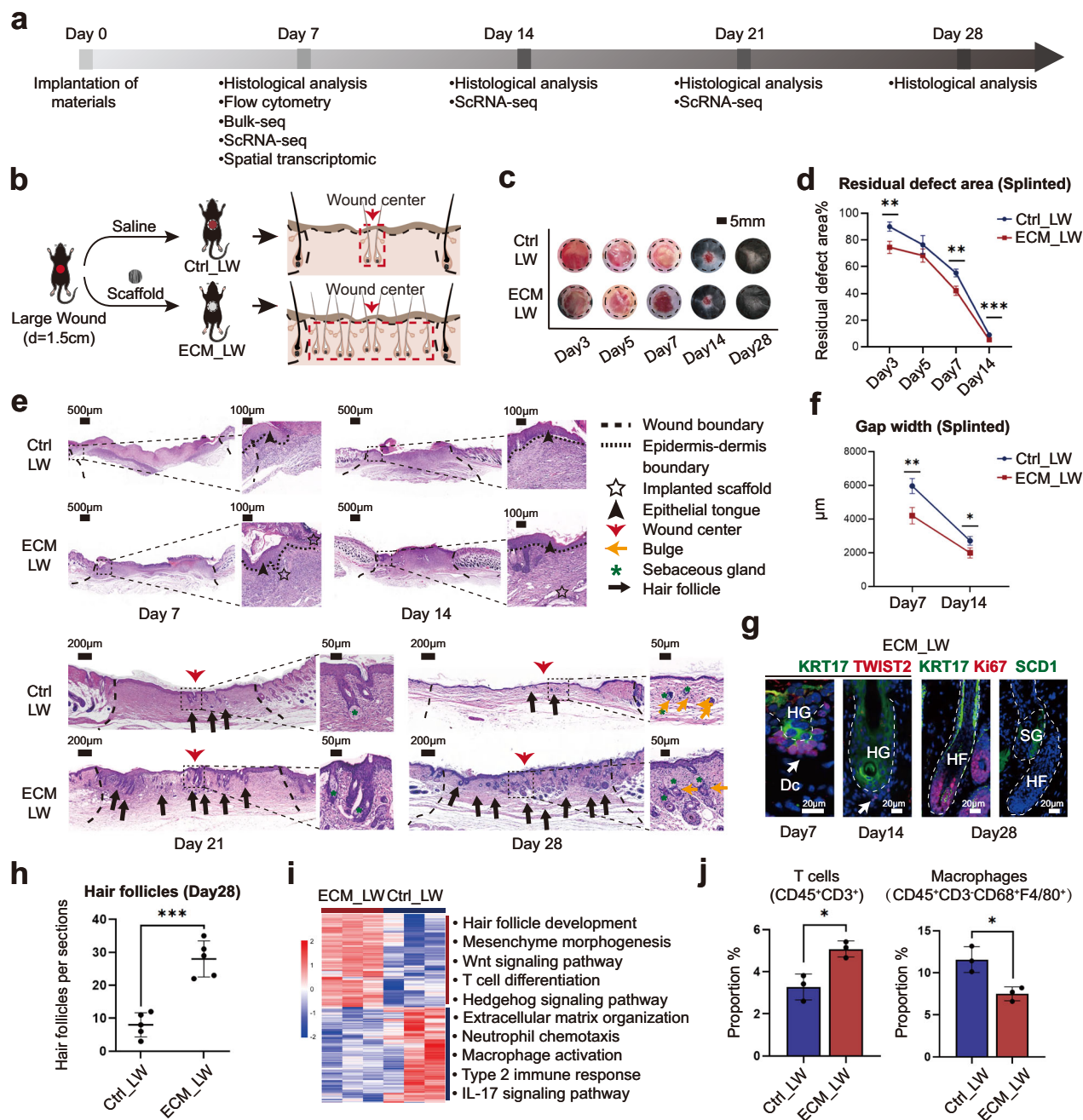


**Fig. 1 | Evaluation of the wound healing process treated with ECM scaffolds.**

**a** Workflow for evaluating large-scale wound healing. **b** Surgical processes for skin splinted excisional wound model. **c** Residual wound area at 3, 5, 7, 14, and 28 days, black dashed circles denoting the original wound area. **d** corresponding analysis of residual wound (Data are presented as mean  $\pm$  SD,  $n = 4$  biologically independent samples, two-tailed t-test, Day3  $**p = 0.002$ ; Day5  $p = 0.104$ ; Day7  $**p = 0.001$ ; Day14  $***p = 0.000444$ ). **e** Representative H&E images of two groups at 7, 14, 21, and 28 days. **f** Quantitative evaluation of the gap width of neo-epithelium (Data are presented as mean  $\pm$  SD,  $n = 4$  biologically independent samples, two-tailed t-test, Day7  $**p = 0.002$ ; Day14  $*p = 0.011$ ). **g** Representative IF images of nascent HF within the ECM\_LW group, stained for KRT17 (green) and TWIST2 (red), Ki67 (red), and SCD1 (green), respectively. Abbreviations: HF, hair follicle; HG, hair germ; Dc, dermal condensate; SG, sebaceous gland. **h** Histologic quantification of de novo

HFs on POD28 (Data are presented as mean  $\pm$  SD,  $n = 5$  biologically independent samples, two-tailed t-test,  $***p = 0.000141$ ). **i** Bulk-RNA sequencing analysis of ECM\_LW versus Ctrl\_LW mice on POD7 ( $n = 3$  for each group). Heatmap (left) showing hierarchical clustering of differentially expressed genes ( $p$  value  $< 0.05$  &  $|\log_2FC| > 1$ ) between two groups, and corresponding gene set enrichment analysis (right) showing the enriched terms in ECM\_LW (top) versus Ctrl\_LW (bottom) groups. **j** Proportions of T cells (CD45<sup>+</sup>CD3<sup>+</sup>) and macrophages (CD45<sup>+</sup>CD3<sup>+</sup>F4/80<sup>+</sup>CD68<sup>+</sup>) cell populations in the wound environment on POD7, determined by flow cytometry (% = the number of target cells / the number of all single live cells) (Data are presented as mean  $\pm$  SD,  $n = 3$  biologically independent samples, two-tailed t-test, T cells  $*p = 0.013$ ; Macrophages  $*p = 0.016$ ).  $p$  value:  $*p < 0.05$ ,  $**p < 0.01$ ,  $***p < 0.001$ , and  $****p < 0.0001$ .

(Fig. 2b). The heterogeneity of keratinocyte subclusters of this dataset corresponded with the healing outcomes of two groups: the higher proportion of *Krt5*<sup>+</sup> interfollicular epidermal basal cell<sup>1</sup> (IFEB<sup>1</sup>) and *Krt10*<sup>+</sup> interfollicular epidermal differentiated cell<sup>1</sup>

(IFED<sup>1</sup>) were observed in the ECM\_LW group on POD7, supporting more neo-epithelium proliferation in the presence of scaffolds in the proliferative stage (Supplementary Fig. 2a). HF neogenesis was believed to occur through the migration of epithelial HFSC or hair

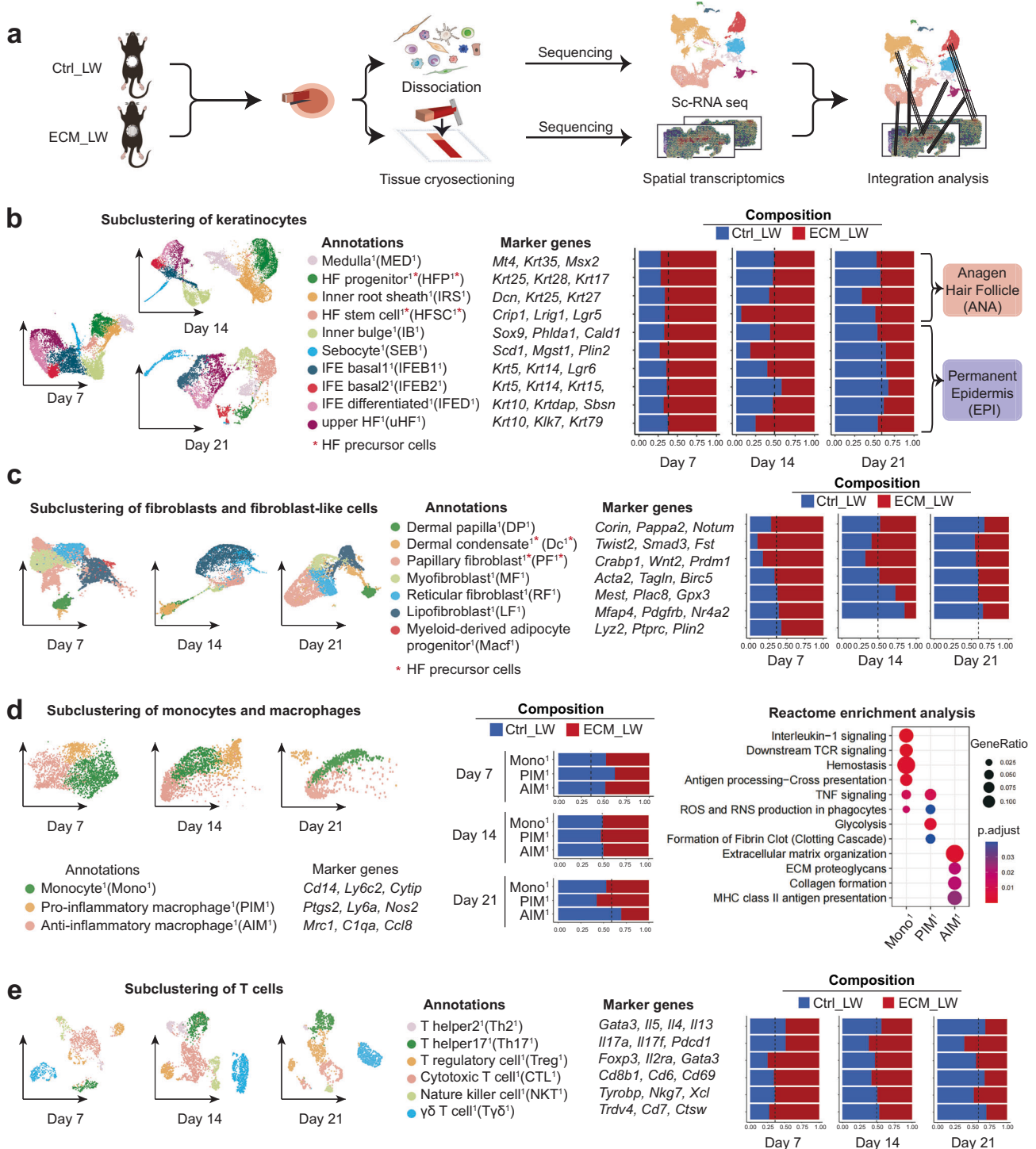


**Fig. 2 | The single-cell atlas of the biomaterials-mediated microenvironment.**

**a** Schematic for generating scRNA-seq and spatial transcriptomics data from large area excisional wounds on POD 7, 14, and 21. **b** Subclustering of keratinocytes showing four subsets from the anagen hair follicle and six subsets from the permanent epidermis. The composition and marker genes for each subset are listed. **c** Subclustering of fibroblasts showing two fibroblast-like subsets and five fibroblast

subsets. The marker genes and composition for each subset are listed.

**d** Subclustering of monocyte/macrophage showing three subsets. The marker genes, composition, and enrichment analysis for each subset are listed.

**e** Subclustering of T cells showing six subsets. The marker genes and composition for each subset are listed.

follicle progenitor (HFP<sup>1</sup>) to the wound center and form the placodes to activate papillary fibroblast (PF) fate specification into dermal condensate (Dc)<sup>40,43,44</sup>. In accordance with reports, we found a higher proportion of *Krt25<sup>+</sup>Krt28<sup>+</sup>Krt17<sup>+</sup>* hair follicle progenitor<sup>1</sup>

(HFP<sup>1</sup>)<sup>22</sup> and *Crip1<sup>+</sup>Lrig1<sup>+</sup>Lgr5<sup>+</sup>* hair follicle stem cell<sup>1</sup> (HFSC<sup>1</sup>)<sup>5</sup> in ECM\_LW group on POD7, 14 and 21 (Fig. 2b), which might serve enough epithelial resources for the following nascent HFs reconstruction.

Fibroblasts are the major mesenchymal cells in the dermal layer of skin, and different fibroblast subclusters occupy distinct locations exhibiting considerable functional diversity. In general, dermis fibroblasts arise from two distinct lineages:<sup>19,45</sup> (1) upper lineage: papillary fibroblast (PF), which contacts the epidermis and gives rise to the dermal component of HFs; (2) lower lineage: reticular fibroblast (RF) which synthesizes most of the ECM protein and lipo-fibroblast (LF) which provides the preadipocytes progenitors of the hypodermis. Besides, skin also contains specialized fibroblast-like cells, including dermal papilla (DP) and dermal condensate (Dc), which have unique transcriptional characteristics with universal fibroblast<sup>46</sup>. DP is located at the base of mature hair follicles and serves as the principal signaling niche of hair follicle activities. Origin from PF, dermal condensate (Dc) is believed to be the progenitor of DP in embryonic development<sup>44,47</sup>. In this dataset, we defined five fibroblasts and two fibroblast-like cells subclusters based on defined markers published before<sup>22,43,48,49</sup> (Fig. 2c). All subclusters expressed pan-fibroblast marker platelet-derived growth factor receptor- $\alpha$  (*Pdgfra*)<sup>43</sup>, while fibroblast-like cells showed the lower expression level of dermatopontin (*Dpt*)<sup>50</sup> and higher expression of pappalysin 2 (*Pappalysin2*)<sup>46</sup> (Supplementary Fig. 5a). In accordance with previous report<sup>43,51</sup>, the primary wave of dermal repair in the Ctrl\_LW group was mediated by the lower lineage fibroblast including *Gpx3*<sup>+</sup>*Mest*<sup>+</sup> reticular fibroblast<sup>1</sup> (RF<sup>1</sup>) and *Mfap4*<sup>+</sup>*Cd34*<sup>+</sup> lipo-fibroblast<sup>1</sup> (LF<sup>1</sup>) on POD7 and POD14, which was respectively related to dermis collagen fibril organization and hypodermis adipocytes formation in GO enrichment analysis (Supplementary Fig. 5b). It's worth noting that RF<sup>1</sup> highly expressed genes enriched in innate immune system, in which *Il33*<sup>52</sup>, *Ira1*<sup>14</sup> and *Il13ra1*<sup>9</sup> were related to the initiation of type 2 macrophage inflammation and collagen deposition in fibrous disease. In contrast, there were more upper lineage *Crabp1*<sup>+</sup>*Prdm1*<sup>+</sup> PF<sup>1</sup> in biomaterial-implanted wounds, which was believed to have the capacity to support HF initiation<sup>48,53</sup> (Supplementary Fig. 5b). Remarkably, we identified the *Twist2*<sup>+</sup>*Smad3*<sup>+</sup> dermal condensate<sup>1</sup> (Dc<sup>1</sup>) cell<sup>44</sup> in this dataset, which was verified by histology (Fig. 1e) and IF (Fig. 1g). In embryologic HF morphology, Dc is acting as the signaling niches to stimulate epithelial placode growth<sup>44</sup>, and thus promote HF morphogenesis. Since there is a significantly higher proportion of Dc<sup>1</sup> and PF<sup>1</sup> in the ECM\_LW group on POD 7 and POD14 (Fig. 2c), which might provide enough mesenchymal component for the subsequent HF formation in the biomaterial-implanted group too.

For the immune micro-environment, most myeloid cells owned the lower proportion in the ECM\_LW group on POD7 (Supplementary Fig. 4b). Firstly, as the first responding immune cells acting as the critical mediators of the innate immune system, neutrophils are necessary for the recruitment and differentiation of monocytes<sup>54</sup>, which were peaked at the early stage. Most neutrophil subclusters owned a higher proportion in the Ctrl\_LW group on POD7 and showed gene enrichment in pro-inflammatory pathways (Supplementary Fig. 6a). There was no noticeable difference in the proportion of dendritic cell (DC) between the two groups on POD7, 14, and 21 (Supplementary Fig. 4b). DC was classified into two subclusters, including *Krts5*<sup>+</sup>*Krt14*<sup>+</sup> Langerhans cell<sup>1</sup> (LC<sup>1</sup>) and *Cd86*<sup>+</sup> monocyte-derived dendritic cell<sup>1</sup> (MDC<sup>1</sup>), respectively related to phagosome and antigen presentation. There was no obvious difference in the proportion of DC subsets between the two groups (Supplementary Fig. 6b).

Monocytes and macrophages (MAC) were vital in biomaterial-related FBR<sup>55</sup>, orchestrating tissue repair by modulating fibroblast activation<sup>9</sup>. Three subsets of MAC, including *Cd14*<sup>+</sup>*Ly6c2*<sup>+</sup> monocytes<sup>1</sup> (Mono<sup>1</sup>), *Ptgs2*<sup>+</sup>*Nos2*<sup>+</sup> pro-inflammatory macrophages<sup>1</sup> (PIM<sup>1</sup>), and *Mrc1*<sup>+</sup>*C1qa*<sup>+</sup> anti-inflammatory macrophages<sup>1</sup> (AIM<sup>1</sup>), were determined (Fig. 2d). As shown in enrichment analysis, pro-inflammatory (classically /M1-like) macrophages can be activated from monocyte by a variety of alarmins, which result in the expression of pro-inflammatory cytokines including TNF and IL-1 $\beta$ . Induced by the IL-4 and IL-13, anti-inflammatory (alternatively activated /M2-like) subsets are the

foremost effectors of type 2 immune response, which play an essential role in aberrant collagen deposition<sup>14</sup> through the expression of TGF- $\beta$  and various matrix remodeling mediators<sup>56</sup>. Of note, AIM<sup>1</sup>, which enriched genes related to collagen formation, was the only subcluster that continuously decreased in the ECM\_LW group on POD 7, 14, and 21, suggesting that the scaffold might play a role in reducing type 2 macrophage infiltration.

Although T cells are not required for wound healing, they are capable of modulating each phase of tissue repair by regulating macrophage activity. T cells were the only immune cell that owned a higher proportion in the ECM\_LW group (Supplementary Fig. 4b), and genes related to T cells were substantially higher expressed by the ECM\_LW group (Supplementary Fig. 4d), suggesting the activation of adaptive immune system induced by biomaterials. Subclustering of T cells resulted in six subsets including *Cd8b1*<sup>+</sup> cytotoxic T cell<sup>1</sup> (CTL<sup>1</sup>), *Tyrbp*<sup>+</sup>*Nkg7*<sup>+</sup>*Xcl*<sup>+</sup> nature killer cell<sup>1</sup> (NKT<sup>1</sup>), *Il17a*<sup>+</sup>*Il17f*<sup>+</sup> T helper1<sup>1</sup> (Th1<sup>1</sup>), *Foxp3*<sup>+</sup>*Gata3*<sup>+</sup> T regulatory cell<sup>1</sup> (Treg<sup>1</sup>), *Trdv4*<sup>+</sup>*Cd7*<sup>+</sup>  $\gamma\delta$ T cell<sup>1</sup> (T $\gamma\delta$ <sup>1</sup>) and *Gata3*<sup>+</sup>*Il4*<sup>+</sup> T helper2<sup>1</sup> (Th2<sup>1</sup>) based on markers from published research<sup>57,58</sup>. More cells in the Th2<sup>1</sup> populations were from the Ctrl\_LW samples on POD7, 14, and 21, whereas the larger number of Treg<sup>1</sup> were from the ECM\_LW samples. *Il4*<sup>+</sup>*Il13*<sup>+</sup> Th2 cells are one of the effector cells associated with type 2 immune responses, which could facilitate the differentiation of type-2 AIM<sup>52</sup>. Located in the dermis near HF in normal skin, regulatory T cells (Tregs) are believed to maintain the balance of immune homeostasis. It has been reported that *Gata3*<sup>+</sup> Tregs could restrain Th2-mediated fibroblast activation and scarring in murine cutaneous fibrosis<sup>42</sup>, and clinical IL-2 therapy (which facilitates Treg proliferation and activation) has also been proven to be effective in alleviating chronic skin fibrosis<sup>59</sup>. In addition, Tregs could also facilitate HFSC differentiation to initiate HF regeneration through Jag1-Notch1 pathways<sup>60</sup>. Gene enrichment analysis confirmed that the Treg<sup>1</sup> subpopulation was enriched in signaling pathways regulating pluripotency of stem cells (Supplementary Fig. 5c), suggesting that Treg<sup>1</sup> recruited by ECM scaffolds might initiate HF neogenesis by both immune-suppression and pro-reparative functions<sup>61</sup>.

### Discovery of spatial heterogeneity around biomaterials

To explore the spatial characteristics of cell heterogeneity in scaffold-implanted wounds, we applied ST to analyze the spatial gene expression profiles. Anatomical structures were identified in the ST sections (Fig. 3a). Based on the gene enrichment analysis of ST (Fig. 3b), the Ctrl\_LW group enriched the genes related to extracellular matrix organization, collagen biosynthetic process, as well as anti-inflammatory (*Mrc1* and *Clec10a*) and oxidative phosphorylation process (*Cox6a2* and *Actn3*) (Fig. 3c), suggesting the typical AIM-driven fibrous tendency in the Ctrl\_LW group. In contrast, the ECM\_LW sample supports a metabolic profile associated with the glycolysis process (*Eno1*, *Gapdh*). Besides, ECM\_LW group expression included gene sets related to the regulation of T cell activation and alpha-beta T cell proliferation that suggested an adaptive immune predominance state in a biomaterial-driven microenvironment (Fig. 3b, c).

To trace the spatial heterogeneity of defined single-cell subclusters, we integrated the expression profiles of sc-RNA seq and ST using AddmoduleScore function<sup>32</sup>. The top 50 (based on avg\_log2FC) marker genes of cutaneous cells in the single-cell dataset (defined in Fig. 2) were scored and projected into the ST slices. The spatial feature plot illustrated keratinocytes crawling around the implanted biomaterials (Fig. 3d), which was verified in Supplementary Fig. 2a. Intriguingly, fibroblasts from different lineages showed a distinct spatial distribution pattern in the Ctrl\_LW group. Upper lineage PF<sup>1</sup> (HF-related) was limited in the upper layer of granulation tissue, while lower lineage RF<sup>1</sup> (fibrous response-related) predominated in the lower layer (Fig. 3e). In contrast, the distribution of PF<sup>1</sup> (HF-related) was enlarged around biomaterials in the ECM\_LW group (Fig. 3e), and ECM\_LW showed the higher expression level of PF<sup>1</sup>

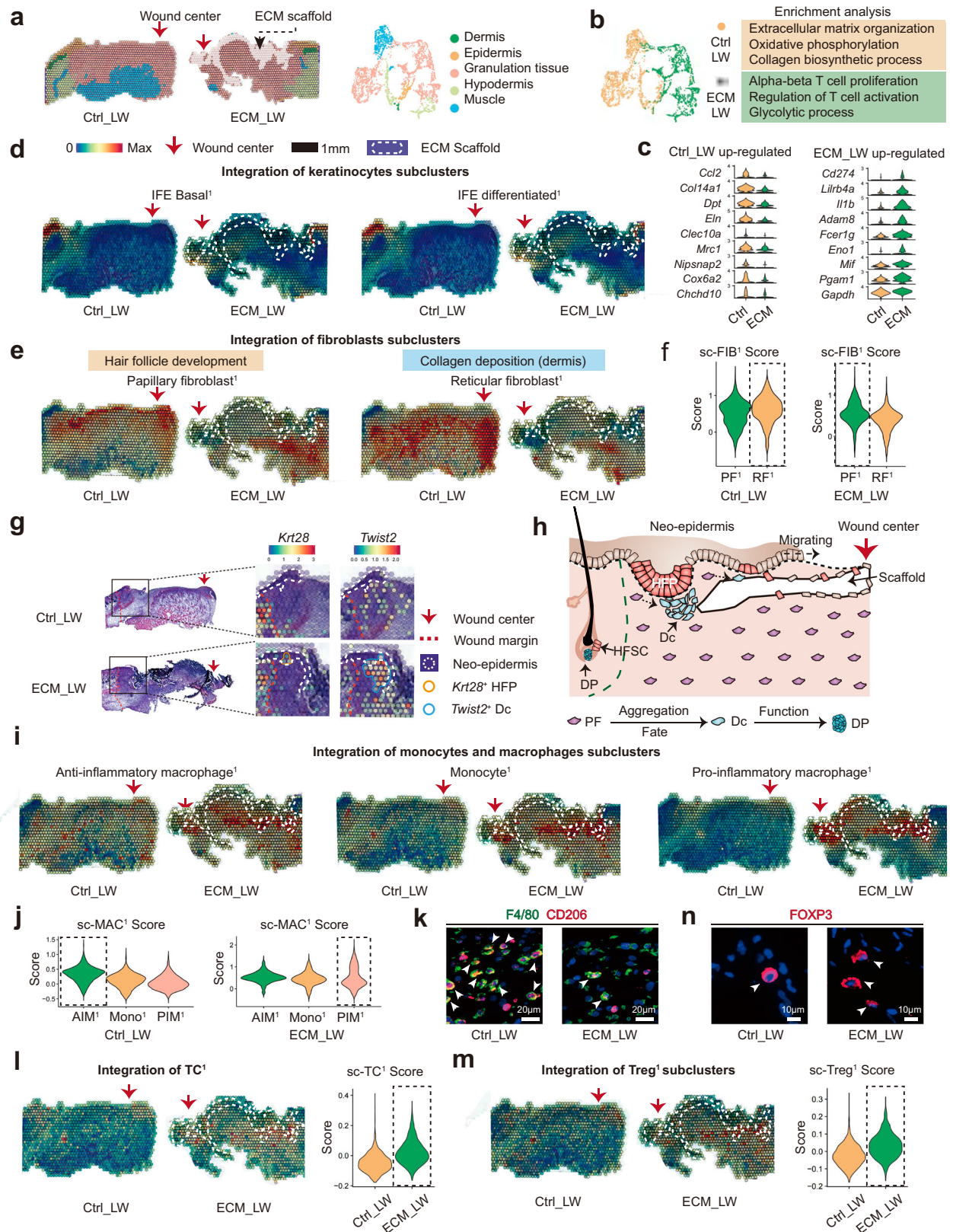


(Fig. 3f), suggesting the pro-regenerative potential of ECM sample. In addition, in the ST profiling of the ECM\_LW group, we identified the initial structure of the hair germ (Fig. 3g) composed of HFP in the neo-epidermis and Dc aggregation beneath the dermis (verified by IF in Fig. 1g), which highlighted the early HF formation signature in the ECM\_LW group at the spatial gene expression level (Fig. 3h).

To assess the spatial characteristics of scaffold-induced immune microenvironment, we integrated the immune cells subclusters (defined in Fig. 2) and ST slices in like manner. Regarding MAC subclusters, ECM showed the ability to reduce the recruitment of AIM<sup>1</sup> (Fig. 3i, j). IF staining of F4/80 and CD206 confirmed the reduced AIM<sup>1</sup> in the ECM\_LW group (Fig. 3k), which might relieve the subsequent

**Fig. 3 | Spatial anchors tracing the cell distribution around the ECM scaffold.** **a** The unsupervised clustering indicated the anatomical structure of samples. **b** Gene enrichment analysis between ECM\_LW and Ctrl\_LW group. **c** Violin plot showing the up-regulated genes of Ctrl\_LW and ECM\_LW samples of ST profile. **d** Spatial feature plot showing the distribution of IFEB<sup>1</sup> and IFED<sup>1</sup> subclusters in tissue sections. **e** Spatial feature plot showing the distribution of PF<sup>1</sup> and RF<sup>1</sup> subclusters in tissue sections. **f** Violin plots of FIB scores of individual spots derived from scRNA-seq data (sc-FIB score) for each subcluster. Dotted boxes stressed clusters with the higher average sc-FIB scores. **g** The spatial feature plot highlighted the expression of *Krt28*<sup>+</sup> hair follicle progenitor and *Twist2*<sup>+</sup> dermal condensate in migrating neo-epidermis. **h** Illustration showing the epithelialization along with de

novo HF formation in the biomaterials-mediated healing process. **i** Spatial feature plot showing the distribution of MAC subclusters in tissue sections. **j** Violin plots of MAC scores of individual spots derived from scRNA-seq data (sc-MAC score) for each subcluster. Dotted boxes stressed clusters with the highest average sc-MAC score. **k** Representative IF images of stained AIM<sup>1</sup> (F4/80<sup>+</sup>CD206<sup>+</sup>), white arrowheads showing the F4/80<sup>+</sup>CD206<sup>+</sup> cells. **l** Spatial feature plot and violin plot showing TC<sup>1</sup> distribution and expression level in tissue sections. **m** Spatial feature plot and violin plot showing the distribution and expression level of Treg<sup>1</sup> in tissue sections. **n** Representative IF images of stained Treg<sup>1</sup> (FOXP3), white arrowheads showing the FOXP3<sup>+</sup> cells.

fibroblast activation and collagen deposition. Instead, we noticed the apparent aggregation of T cells (Fig. 3l), especially Treg<sup>1</sup> (Fig. 3m), colocalized with PF<sup>1</sup> (HF-related) surrounding the biomaterial. The recruitment of Treg<sup>1</sup> (confirmed by IF in Fig. 3n) might contribute to the suppression of the type-2 immunity activated by AIM<sup>1</sup>.

### Prediction of critical signaling patterns between spatially co-localized cell populations around the biomaterial

Based on the multimodal profiling, we observed a higher proportion of T cells (the schematic summary was shown in Fig. 4a) and HF precursor cells in the ECM\_LW group, which implied a potential cellular communication among them. Next, we applied CellChat to predict the cell-cell communication patterns of immune cells and cutaneous cells between ECM\_LW and Ctrl\_LW groups. The circle plots showed the overall interaction number of the ligand-receptors in the Ctrl\_LW and ECM\_LW groups (Fig. 4b). An intensive communication network between fibroblasts and immune cells was observed in both groups. The more abundant interactions in the Ctrl\_LW group appeared to be sent from the RF<sup>1</sup>, LF<sup>1</sup>, MF<sup>1</sup>, and Mac<sup>1</sup> subpopulations, indicating the predominance of fibrotic fibroblasts interaction signals in the dermis. In contrast, the more abundant interactions in the ECM\_LW group were sent from the Dc<sup>1</sup> and PF<sup>1</sup> subpopulations, indicating the pro-regenerative signals induced by biomaterials. Since AIM<sup>1</sup> might be the major immune cells contributing to tissue fibrosis, we compared specific interactions among AIM<sup>1</sup> and fibroblast subpopulations (Fig. 4c). The interaction of AIM<sup>1</sup> with fibrotic fibroblasts was more noted in the Ctrl\_LW group via *Tgfb1*–(*Tgfb2*+*Acvr1b*) binding, which play potential pro-fibrotic roles on the target cells<sup>33</sup>. In comparison, the interaction of Treg<sup>1</sup> with HFSC was more noted in the ECM\_LW group via *Jag1*–*Notch1* binding, suggesting the pro-regenerative role of Treg<sup>1</sup> in biomaterial-treated wounds<sup>60</sup>. Of note, we detected the more significant interactions of Treg<sup>1</sup> with PIM<sup>1</sup> and Mono<sup>1</sup> via *Jag1*–*Notch2* binding. It has been reported the essential role of Notch signaling in macrophage polarization. Selective inhibitors of Notch signaling significantly suppressed M1-like macrophages and up-regulated the M2-like macrophages<sup>62</sup>. Consistent with the gene expression profile at the single-cell level, we confirmed the potential *Jag1*–*Notch2* communication in ST profiles (Fig. 4e). Prominent *Notch2* expression was observed around implanted biomaterial, implicating the suppressive role of Tregs in the scaffold-mediated microenvironment.

### The adaptive immune system was required for the skin regeneration mediated by ECM scaffolds

To determine the role of the adaptive immune system in HF regeneration, we placed ECM scaffolds in the dorsal skin of immunodeficient C57Bl/6 (B6.129-Rag2tm1) mice, which lacked mature T lymphocytes<sup>63,64</sup> (Fig. 5a). We noticed that the wound closure rate was delayed on POD7 (Fig. 5b–d), and regeneration of HF was scarce (Fig. 5b, e) on day 28 in Rag2<sup>-/-</sup> mice. Compared to wildtype (WT) mice, Rag2<sup>-/-</sup> group still possessed a myeloid recruitment ability, but no visible accumulation of T cells around biomaterials was observed (Supplementary Fig. 7). Next, we further explored the differences in cell composition and spatial gene expression between WT and Rag2<sup>-/-</sup> mice using scRNA-seq

(Supplementary Fig. 8). As shown in Fig. 5f, in accordance with the HF regeneration outcomes, the Rag2<sup>-/-</sup> group reduce the proportion of PF<sup>2</sup> (related to HF development) but improve the number of RF<sup>2</sup> (related to collagen deposition) and LF<sup>2</sup> (related to collagen deposition and angiogenesis). For the immune microenvironment, the Rag2<sup>-/-</sup> samples recruited fewer T cells but more monocyte/macrophages than the WT group (Supplementary Fig. 8b). T cell related genes such as *Areg*, *Trdc*, and *Rgs2* were down-regulated in Rag2<sup>-/-</sup> samples (Supplementary Fig. 8c). The proportion of neutrophil and dendritic cell subsets was basically equilibrium between the two groups (Supplementary Fig. 9). Subclustering of MAC resulted in three subsets including PIM<sup>2</sup>, AIM<sup>2</sup>, and Mono<sup>2</sup> (Fig. 5g). Rag2<sup>-/-</sup> samples improved the recruitment of AIM<sup>2</sup>, PIM<sup>2</sup>, in which AIM<sup>2</sup> owned the highest proportion (46.2%). Subclustering of T cells resulted in seven subsets (Fig. 5h). The Rag2<sup>-/-</sup> groups contributed to fewer T cells in most subsets except NKT<sup>2</sup> (related to natural killer cell-mediated cytotoxicity) and naive Th<sup>2</sup>, indicating the dysfunctional adaptive immune systems in Rag2<sup>-/-</sup> group. The absence of suppressive Treg<sup>2</sup> might be the reason for uncontrolled type-2 AIM<sup>2</sup> accumulation and collagen deposition of fibrotic RF<sup>2</sup>.

To explore the spatial characteristics of cell heterogeneity in immunodeficient mice, we also applied ST to analyze the spatial gene expression profiles. Anatomical structures could be identified in the ST sections (Fig. 6a). Based on the gene enrichment analysis of ST, the Rag2<sup>-/-</sup> sample down-regulated gene expression in hair follicle morphogenesis but improved the genes related to collagen fibril organization (Fig. 6b). Compared to WT samples, the distribution and expression level of PF<sup>2</sup> (HF-related) was reduced (Fig. 6c), which was verified by the IF staining of the corresponding marker gene *Crabp1* (Fig. 6d). In contrast, the distribution and expression level of lower lineage *Mest*<sup>+</sup> RF<sup>2</sup> were significantly increased (Fig. 6e, f), in accordance with the healing outcome of Rag2<sup>-/-</sup> groups. To compare the scaffold-induced immune microenvironment, we also integrated marker genes of immune cells (defined in Fig. 5) with ST profiling. We confirmed the more obvious aggregation of AIM<sup>2</sup> surrounding the biomaterial in the Rag2<sup>-/-</sup> sample (Fig. 6g, h), which might contribute to the absence of the Treg<sup>2</sup> (Fig. 6i, j).

### Biomaterials facilitate de novo HF regeneration despite wound size

To detect any differences in wound healing between small and large wounds treated with biomaterials, we repeated the experiment with small (diameter=0.6 cm) full-thickness wounds implanted with biomaterials (Fig. 7a, b). Consistent with the ECM\_LW group, the scaffold implanted in the small wound (ECM\_SW) did not trigger an obvious FBR fibrous capsule and had a rapid degradation rate (Fig. 7c). Histological sections of ECM\_SW tissue revealed clear signs of enhanced HF reconstruction too (Fig. 7c, d). ST was also applied to explore the spatial characteristics of Ctrl\_SW and ECM\_SW samples, and the anatomical structure was shown in Fig. 7e. We still observed the recruitment of Cd3<sup>+</sup> T cells around the implanted biomaterial, which were colocalized with *Crabp1*<sup>+</sup> papillary fibroblasts in ECM\_SW sample (Fig. 7g), confirming the pro-regenerative potential of ECM scaffolds despite of wound size.

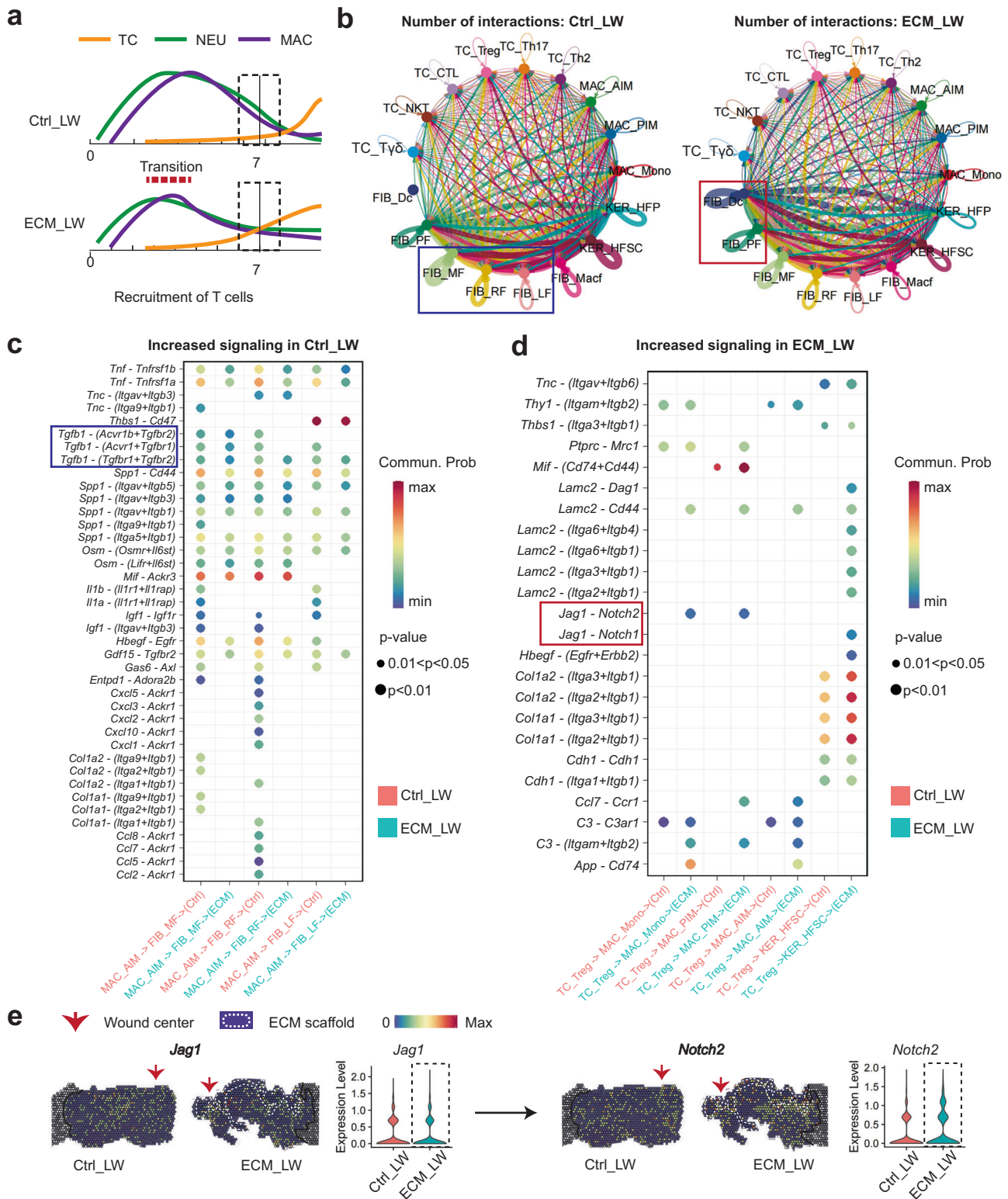


**Fig. 4 | Cellular communication landscape between immune cells and cutaneous cells.** **a** Schematic timeline highlighting the recruitment of immune cells from innate and adaptive immune systems in Ctrl\_LW (top) and ECM\_LW (bottom) groups. **b** Comparison of overall cell-cell interaction numbers of immune cells and cutaneous cells between Ctrl\_LW and ECM\_LW using CellChat. **c** The

ligand–receptor pairs up-regulated in the Ctrl\_LW group in specificity between AIM<sup>+</sup> and fibroblasts (MF<sup>+</sup>, RF<sup>+</sup>, and LF<sup>+</sup>). **d** The ligand–receptor pairs up-regulated in the ECM\_LW group in specificity between Treg<sup>+</sup>, MAC (Mono<sup>+</sup>, PIM<sup>+</sup>, AIM<sup>+</sup>), and HFSC<sup>+</sup>. **e** Spatial feature plots and corresponding violin plots showed the expression level of the ligand and cognate receptor in the Notch signaling pathway.

### Discussion

Synthetic graft transplantation is an efficient treatment for severe large-area skin wounds, especially when the donor site is not qualified<sup>18</sup>. With an additional understanding of tissue engineering, it is

suggested that synthetic biomaterials imitating the native structure of ECM can integrate and potentially play a pro-regenerative role in wound healing<sup>20,65</sup>. The reconstruction of dermal appendages is an essential indicator of complete skin regeneration. Nevertheless,



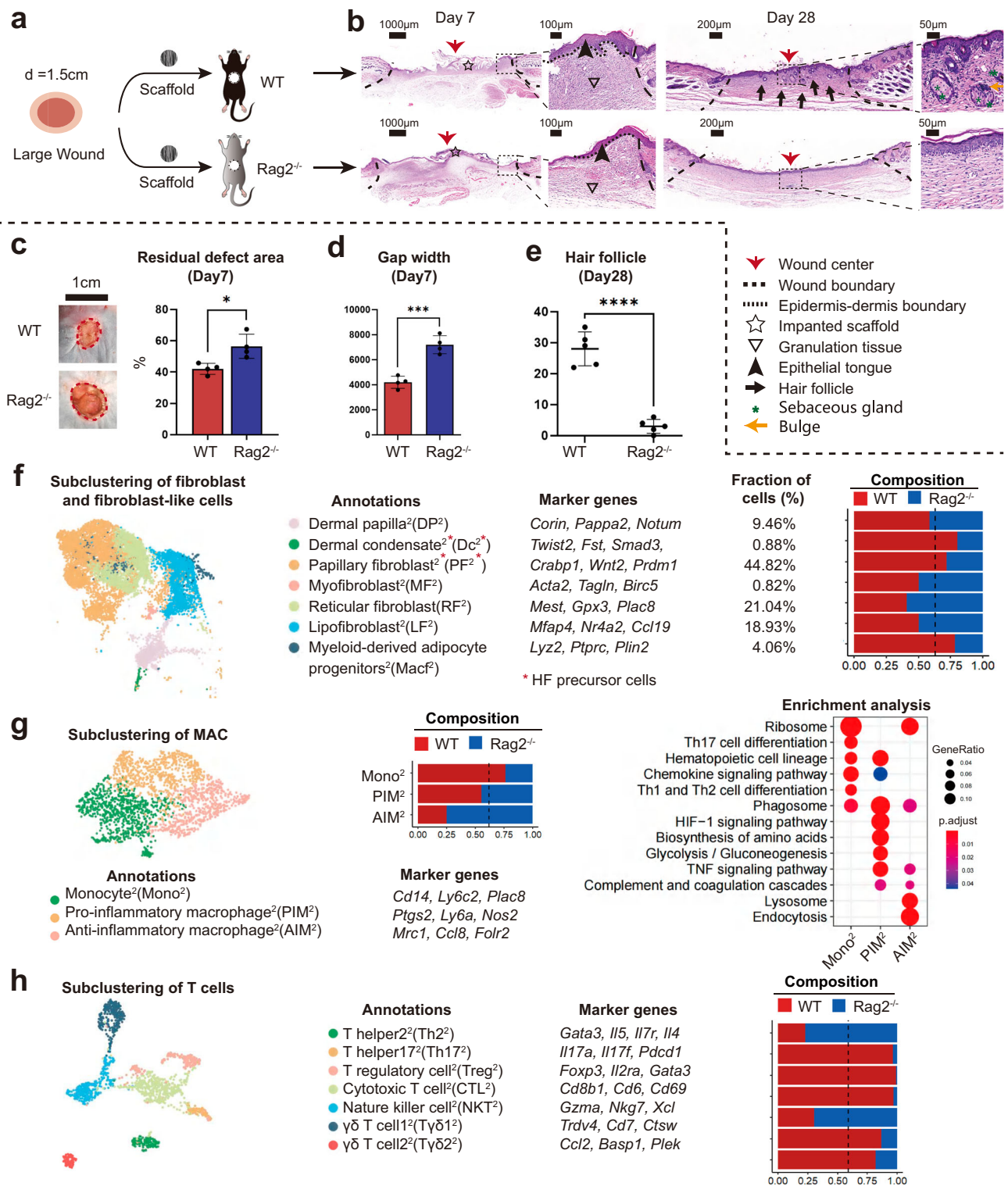


**Fig. 5 | Evaluation of wound healing in immunodeficient mice lacking mature T cells.** **a** The surgical process for evaluating large area wound healing mediated by ECM scaffold in WT and Rag2<sup>-/-</sup> mice. **b** Representative histological images of wound healing in WT and Rag2<sup>-/-</sup> mice at 7 and 28 days. **c** Residual defect area on POD 7 (Data are presented as mean ± SD, n = 4 biologically independent samples, two-tailed t-test, \*p = 0.014). **d** Semiquantitative evaluation of gap width (Data are presented as mean ± SD, n = 4 biologically independent samples, two-tailed t-test, \*\*\*p = 0.00046). **e** Histologic quantification of de novo HFs (Data are presented as

mean ± SD, n = 5 biologically independent samples, two-tailed t-test, \*\*\*\*p = 0.000013). **f** Subclustering of fibroblasts and fibroblast-like cells showing two fibroblast-like subsets and five fibroblast subsets. Marker genes for fibroblast subsets are listed. **g** Subclustering of monocyte/macrophage showing three subsets. The marker genes, composition, and enrichment analysis for each subset are listed. **h** Subclustering of T cells showing seven subsets. The marker genes and composition for each subset are listed. p value: \*p < 0.05, \*\*p < 0.01, \*\*\*p < 0.001 and \*\*\*\*p < 0.0001.

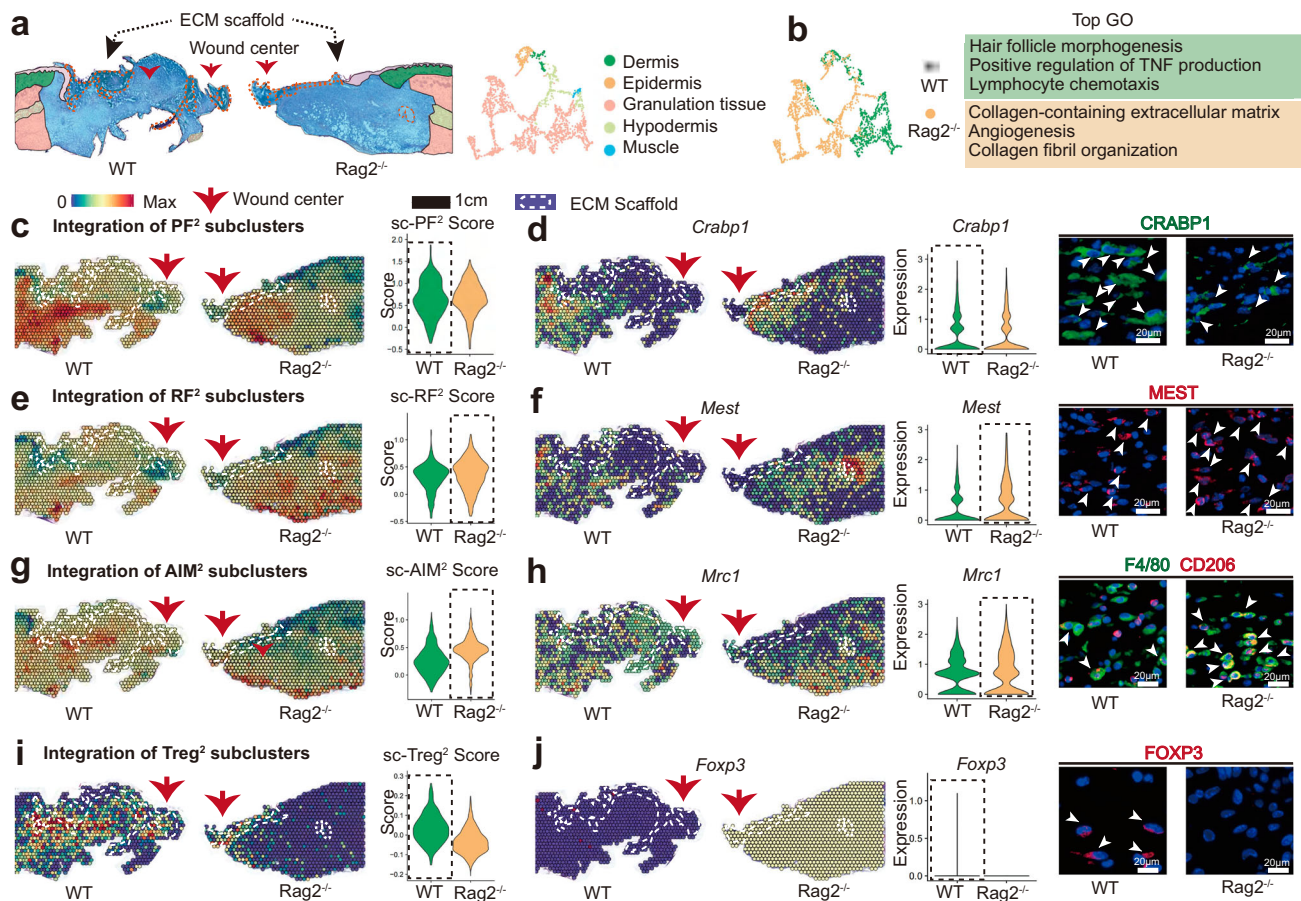


**Fig. 6 | Spatial atlas of cell microenvironment around biomaterials of immunodeficient mice. a** The anatomical structure of each sample. **b** Gene enrichment analysis between WT and Rag2<sup>-/-</sup> group. **c** Spatial feature plot and violin plot showing the distribution and expression level of integrated PF<sup>2</sup> subcluster in tissue sections. **d** Spatial feature plot and violin plot showing the distribution and expression level of *Crabp1* (marker gene of PF<sup>2</sup>) in tissue sections; Representative IF images of stained PF<sup>2</sup> (CRABP1<sup>+</sup>), white arrowheads showing the CRABP1<sup>+</sup> cells. **e** Spatial feature plot and violin plot showing the distribution and expression level of integrated RF<sup>2</sup> subcluster in tissue sections. **f** Spatial feature plot and violin plot showing the distribution and expression level of *Mest* (marker gene of RF<sup>2</sup>) in tissue sections; Representative IF images of stained RF<sup>2</sup> (MEST<sup>+</sup>), white arrowheads

showing the MEST<sup>+</sup> cells. **g** Spatial feature plot and violin plot showing the distribution and expression level of integrated AIM<sup>2</sup> subcluster in tissue sections. **h** Spatial feature plot and violin plot showing the distribution and expression level of *Mrc1* (marker gene of AIM<sup>2</sup>) in tissue sections; Representative IF images of stained AIM<sup>2</sup> (F4/80<sup>+</sup> CD206<sup>+</sup>), white arrowheads showing the F4/80<sup>+</sup> CD206<sup>+</sup> cells. **i** Spatial feature plot and violin plot showing the distribution and expression level of integrated Treg<sup>2</sup> subcluster in tissue sections. **j** Spatial feature plot and violin plot showing the distribution and expression level of *Foxp3* (marker gene of Treg<sup>2</sup>) in tissue sections; Representative IF images of stained Treg<sup>2</sup> (FOXP3<sup>+</sup>), white arrowheads showing the FOXP3<sup>+</sup> cells.

existing treatments can only form epidermal or dermal layers and fail to regenerate enough HF and SG<sup>66</sup>. Requirements for the promotion of nascent HF formation bring significant challenges to biomaterial design, particularly for large-scale severe wounds.

Here, the pro-regenerative influence of the adaptive immune system in coordinating wound repair has been stressed<sup>12</sup>. We employed an ECM scaffold for large-area skin defects and investigated its immunoregulatory mechanism in wound healing. The scaffold showed an impact by accelerating wound closure and promoting nascent HF formation (Fig. 1c–g). By multimodal analysis, we observed the substantial accumulation of type 2 immune cells (especially *Mrc1*<sup>+</sup> AIM and *Gata3*<sup>+</sup> Th2 cells) in Ctrl\_LW samples (Fig. 2d, e), which might promote the fast healing of damaged tissue at the expense of the original skin composition and function<sup>67,68</sup>. In contrast, adaptive T cell infiltration in response to scaffold implantation was driven towards immunosuppression subpopulations in the ECM\_LW group. A larger number of *Foxp3*<sup>+</sup> Tregs were recruited by ECM scaffold to mitigate skin fibrosis by suppressing excessive type 2 macrophage inflammation (Figs. 2e and 3l–m). We

next confirmed the requirement of T cells in skin regeneration by an immunodeficient model (Fig. 5). The absence of suppressive Treg<sup>2</sup> might be one of the reasons for the uncontrolled accumulation of type-2 AIM<sup>2</sup>, which might drive collagen deposition by activating profibrotic RF<sup>2</sup>. These data validated that the activation of adaptive immune was required for the reparative effect mediated by ECM scaffolds. Meanwhile, mild FBR around the scaffold decreased the risk of immune rejection, and the appropriate degradation rate could also avoid the extra expense of secondary surgery in both small and large-area wound healing (Fig. 7).

In this study, we offered an available manner for large-area wound regeneration and first defined the spatial heterogeneity of the microenvironment during the biomaterial-mediated wound healing process. These techniques provided a unique medium through which we can further understand the immunoregulatory mechanisms of the ECM scaffold. Of note, we testified the role of the adaptive immune system activated by biomaterials in HF reconstruction and provided further insights into the future design of targeted immunoregulatory materials for scarless wound regeneration.

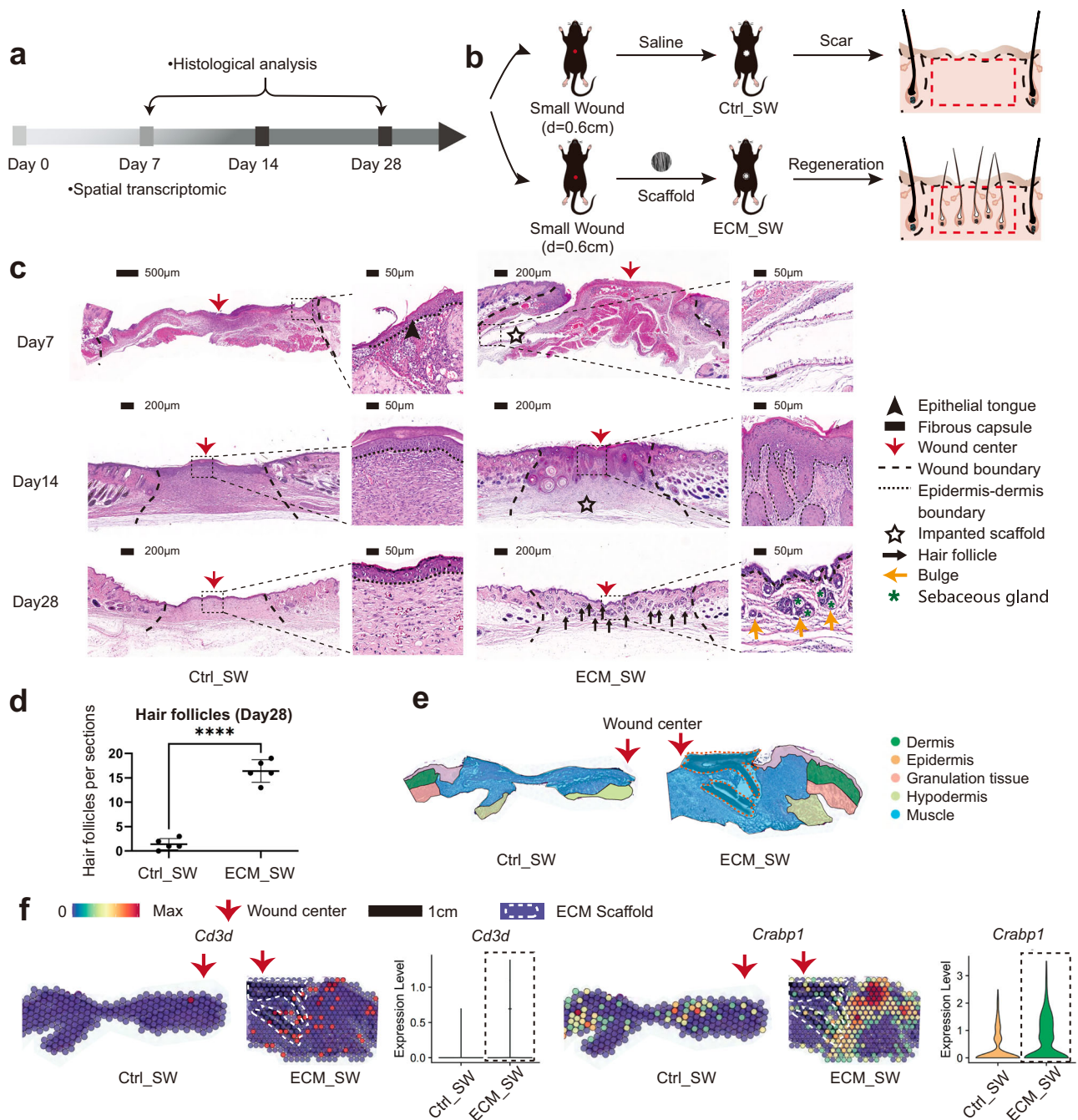


**Fig. 7 | Evaluation of the healing of small full-thickness wounds treated with ECM scaffolds.** **a** Workflow for evaluating skin wound healing. **b** The surgical process for skin excisional wound model of Ctrl\_SW and ECM\_SW group. **c** Representative H&E images of Ctrl\_SW and ECM\_SW samples. **d** Histologic quantification of de novo HF on POD28 (Data are presented as mean  $\pm$  SD,  $n = 5$

biologically independent samples, two-tailed t-test, \*\*\*\* $p = 0.000001$ ). **e** The anatomical structure of samples. **f** Spatial feature plot showing the expression of *Cd3d* (marker gene of T cells) and *Crabp1* (marker gene of papillary fibroblasts) in ST profile and corresponding quantitative analysis.  $p$  value: \* $p < 0.05$ , \*\* $p < 0.01$ , \*\*\* $p < 0.001$ , and \*\*\*\* $p < 0.0001$ .

## Methods

### Ethical approval

All procedures were approved by the Institution Review Board of West China Hospital of Stomatology (No. WCHSIRB-D-2020-385).

### Fabrication of ECM scaffolds

To fabricate the electrospinning scaffold with approximate 300 nm diameter aligned fibers, 20% w/v PLGA (LA/GA = 75:25, molecular weight = 105 kDa, Jinan Daigang Biomaterial Co. Ltd.) and 2% w/v FC (Sangon Biotech Co. Ltd.) were dissolved in HFIP (Aladdin Co., Ltd.) with stirring until complete dissolution. The solution was fed at

0.018 mm/min, and a voltage of  $-2/5$  kv and 11 cm distance between the needle (21 G) and the rotating cylinder (2800 rpm) was applied. After been dried in a vacuum oven for a week. The morphology of PLGA/FC nanofibrous scaffold was observed by scanning electron microscopy (SEM; JSM-7500F, JEOL, Japan). The scaffolds were cut into circular shapes (0.8 cm or 1.8 cm in diameter) and sterilized using  $\gamma$ -irradiation before the animal implantation experiments.

### Excisional wound model and implantation procedures

All procedures involving animals were approved by the Institution Review Board of West China Hospital of Stomatology

(No. WCHSIRB-D-2020-385). Female wildtype C57BL/6J mice (Dossy Experimental Animals Co., Ltd.) and immunodeficient C57BL/6 (B6.129-Rag2tm1) mice (Shanghai Model Organisms Center Inc., Shanghai, China), at the age of 6–8 week (~20 g) were used in this research. The mice were housed under standard conditions including temperature of 21–27 °C, humidity of 40–70%, and a 12 h light-dark cycle with free access to food. The number of animals used for each experiment is indicated in the figure legends. To minimize wound contraction by the panniculus carnosus of rodents and allow wound healing through granulation and re-epithelialization like the human skin, we use the mice-splinted model<sup>36</sup>. The circular (diameter = 0.6 or 1.5 cm) full-thickness wounds were created in the mice dorsal skin and stented by silicone loops. The mice in further study were divided into three groups: large wound (diameter = 1.5 cm) treated with saline (Ctrl\_LW) or ECM scaffolds below the wound (ECM\_LW), and small wound (diameter = 0.6 cm) treated with ECM scaffolds (ECM\_SW). Subsequently, the wounds were covered with sterile Tegaderm film (3M) and respectively fixed on the small (inner diameter 8 mm and outer diameter 12 mm, for small wound) or large (inner diameter 18 mm and outer diameter 22 mm, for large wound) silicone ring with uniform suture. Mice were euthanized at 1–4 weeks after the surgery, and the small (diameter 10 mm, for small wound) or large (diameter 25 mm, for large wound) round full-thickness sample was harvested.

### Bulk-RNA sequencing

Three replicates of mice skin wounds in each group were collected for the of bulk-tissue RNA sequencing procedure. Total amounts and integrity of RNA were assessed using the RNA Nano 6000 Assay Kit of the Bioanalyzer 2100 system (Agilent Technologies, CA, USA). mRNA was purified from total RNA by using poly-T oligo-attached magnetic beads. The library fragments were purified with AMPure XP system (Beckman Coulter, Beverly, USA). The PCR amplification product was purified by AMPure XP beads. After the library is qualified by qRT-PCR, the different libraries are pooling and being sequenced by the Illumina NovaSeq 6000. FeatureCounts (v1.5.0-p3) was used to count the reads numbers mapped to each gene. And then FPKM of each gene was calculated based on the length of the gene and reads count mapped to this gene. Differential expression analysis of two groups (three biological replicates per group) was performed using the DESeq2 R package (v1.32.0),  $p$  value < 0.05, and  $|\log_2(\text{foldchange})| > 2$  was set as the threshold for significantly differential expression. Gene enrichment analysis was performed using ClusterProfiler (v4.6.2) and org.Mm.eg.db (v3.13.0). GO terms and KEGG pathways with corrected  $p$  value less than 0.05 were considered significantly enriched by differentially expressed genes. Chord plots and heatmap of differentially expressed genes were plotted by GOplot (v1.0.2) and ggplot2 (v3.4.2).

### Single cell RNA sequencing

**Tissue dissociation.** Three fresh samples were collected per group for scRNA-seq. In brief, the wound tissues were firstly digested by the Epidermis Dissociation Kit (Epidermis Dissociation Kit, mouse; Miltenyi Biotec) for enzymatic epidermal-dermal separation. The epidermis part was dissociated by a gentleMACS Dissociator (Miltenyi), then filtered (70- $\mu$ m cell strainer, Corning, Durham), centrifuged (300 g, 10 min, 4 °C), and resuspended with phosphate-buffered saline (PBS) containing 0.5% bovine serum albumin (BSA). The dermis part was cut into 1 mm width pieces and mixed with mixed enzyme solution containing type I collagenase (Gibco, Grand Island) and trypsin (Gibco, Canada), then dissociated by gentleMACS Dissociator (Miltenyi), and digested for 2.5 hours in a hybridization oven (Peqlab PerfectBlot). After being dissociated, filtered, centrifuged, and resuspended in red blood cell lysis buffer (Solarbio), the dermis cells were mixed with the epidermis part. Then the dead cells and debris were removed by Dead Cell Removal MicroBeads (Miltenyi).

**Sequencing and data processing.** Single-cell suspensions were then carried out for Single-Cell RNA-seq (10x Genomics Chromium Single Cell Kit). Sequencing (10x Genomics Chromium Single Cell 3' v3) was performed using an Illumina 1.9 mode. Then, reads were aligned, and expression matrices were generated for downstream analysis (Cell Ranger pipeline software).

**Downstream computational analysis.** Different samples were merged into one Seurat object using the RunHarmony function of harmony R packages (v0.1.1) to correct the potential batch effect. Filtering, normalization, scaling, and canonical correlation analysis were performed with the Seurat R package (v4.1.0). RunPCA function was used to process the most variable genes determined by the FindVariableGenes function (selection.method = "vst", nfeatures = 4000). ElbowPlot function was performed to determine the number of principle components input. RunUMAP function (Seurat) with the first 20 principal components as input was performed for dimensionality reduction. Unsupervised clustering was performed using the FindClusters function of Seurat and clustree R package (v0.5.0) and differentially expressed genes were determined by the FindAllMarkers function for cluster annotation. ClusterProfiler (v4.6.2) was used to perform the gene set enrichment analysis. CellChat (v1.5.0) was used to predict receptor-ligand probability among cell subpopulations.

### Spatial transcriptomics

**Slide preparation.** Fresh samples were rapidly harvested and frozen in OCT. Wound tissues were cryosectioned at -20 degrees onto gene expression slides. Tissue sections on the Capture Areas of the Visium Spatial Gene Expression are fixed using methanol, H&E staining images will be used downstream to map the gene expression patterns. Using the Visium Tissue Optimization Slide & Reagent kit, permeabilization time was optimized. Second Strand Mix is added to the tissue sections to initiate second strand synthesis. After the transfer of cDNA from the slide, spatially barcoded, full-length cDNA is amplified via PCR to generate sufficient mass for library construction. The final libraries contain the P5 and P7 primers used in Illumina amplification. A Visium Spatial Gene Expression library comprises standard Illumina paired-end constructs that begin and end with P5 and P7. Raw FASTQ files and histology images were processed (SpaceRanger software) for genome alignment.

**Downstream computational analysis.** Raw output files for each group were read into R studio with the Seurat R package (v4.1.0). Normalization across spots was performed with the SCTransform function. The spatial cluster gene signature overlap correlation matrix was generated by first taking all genes differentially expressed ( $\text{avg\_log2FC} > 1$  and adjusted  $p$  value < 0.05) across all ST clusters.

**Integration analysis of scRNA-seq and ST.** Signature scoring derived from scRNA-seq and ST signatures was performed with the AddModuleScore function in Seurat R packages (v4.1.2)<sup>32</sup>. Firstly, the FindAllMarkers function was used to identify the top 50 marker genes (based on  $\text{avg\_log2FC}$  value) of each cluster on the single-cell level. AddModuleScore was then used to calculate the average expression of each gene set in each spot of the spatial transcriptome. Finally, the scores were mapped to the spatial transcriptome using the SpatialFeaturePlot function, and quantitative assessment was performed using the ggviolin function in ggplot2 R packages (v3.4.2).

**R analysis packages.** R v4.1.0 was used for downstream analysis of single-cell RNA sequencing and spatial transcriptomics data. R packages used: Seurat(v4.1.0), harmony (v0.1.1), clustree (v0.5.0), tidyverse (v2.0.0), Matrix (v2.0.0), ggplot2 (v3.4.2), DESeq2 (v1.32.0), GOplot (v1.0.2), reshape2 (v1.4.4), stringr (v1.5.0), EnhancedVolcano (v1.10.0),

ClusterProfiler (v4.6.2), org.Mm.eg.db (v3.13.0), Cellchat (v1.5.0), patchwork (v1.1.2), data.table (v1.14.8), hdf5r (v1.3.8), pracma (v2.4.2). The tutorial of Seurat software is available at <https://satijalab.org/seurat/index.html>. The tutorial of ClusterProfiler software is available at <https://github.com/YuLab-SMU/clusterProfiler>. The tutorial of GOpot software is available at <https://github.com/cran/GOpot>. The tutorial for EnhancedVolcano software is <https://github.com/kevinblighe/EnhancedVolcano>. The tutorial on Cellchat software is available at <https://github.com/sqjin/CellChat>.

**Histopathology, Immunohistochemistry, and immunofluorescence microscopy.** The samples were fixed with 4% paraformaldehyde at least 48 hours before ethanol and xylene dehydration. H&E staining and Masson's trichrome staining were performed for the observation of re-epithelialization and collagen fiber deposition. Immunofluorescence staining for cytokeratin 5 (ab52635, Abcam, 1:200), cytokeratin 10 (ab76318, Abcam, 1:150), cytokeratin 17 (17516-1-AP, Proteintech, 1:200), TWIST2 (66544-1-Ig, Proteintech, 1:100), Ki67 (Servicebio, GB121141, 1:100), SCD1 (28678-1-AP, Proteintech, 1:200), CRABP1 (13163 S, Cell Signaling, 1:100), MEST (11118-1-AP, Proteintech, 1:100) were performed for to assess wound regeneration. For the evaluation the infiltration of immune cells, immunohistochemistry staining for CD3 (14-0032-82, Thermo Fisher Scientific, 1:100), CD68 (ab283654, Abcam, 1:100), Ly6G (ab238132, Abcam, 1:2000) and immunofluorescent staining for F4/80 (29414-1-AP, Proteintech, 1:200), CD206 (360017, Zenbio, 1:100), FOXP3 (sc-53876, Santa Cruz Biotechnology, 1:100), were performed.

**Flow cytometry analysis.** Single cells digested from skin wounds were pre-incubated with purified anti-CD16/CD32 antibody (101301, BioLegend) (1.0  $\mu$ g per  $10^6$  cells in 100  $\mu$ l volume) for 5 to 10 min to block Fc receptors. The cell suspensions were then co-incubated with fixable viability dye (eFluor™ 780, 65-0865-14, eBioscience) and antibodies against surface markers CD45 (PE/Cyanine7, 147703, BioLegend), CD3 (PE, 100205, BioLegend), and F4/80 (FITC, 123107, BioLegend) at 1:400 dilution for 30 min at 4 °C in the dark (100  $\mu$ l per antibody per sample). After fixation and permeabilization, cells were incubated with antibodies against intracellular marker CD68 (APC, 137007, BioLegend) at 1:400 dilution for 20 min at 4 °C in the dark (100  $\mu$ l per antibody per sample). Isotype controls of CD45 (PE/Cyanine7 Rat IgG2b,  $\kappa$ , 400617, BioLegend), CD3 (PE Rat IgG2b,  $\kappa$ , 400607, BioLegend), F4/80 (FITC Rat IgG2a,  $\kappa$ , 400505, BioLegend) and CD68 (APC Rat IgG2a,  $\kappa$ , 400511, BioLegend) were used in same concentration. Flow cytometry analysis was performed using Attune Nxt flow cytometer (Thermo Fisher Scientific) and FlowJo (v10.8.1). The experiments were performed three times independently ( $n = 3$ ).

**Statistics and reproducibility.** The precise sample number for each experiment was indicated in the figure legends. For Figs. 1g, 3k, 3n, 6d, 6f, 6h, and 6j, representative images were shown from one of three biological repeats; For Fig. 5b and Supplementary Fig. 2a, representative images were shown from one of four biological repeats; For Figs. 1e, 7c and Supplementary Fig. 1c, 2d, 7a, representative images were shown from one of five biological repeats. The data was dealt with Case Viewer software, Image J software, and Prism 8.0 software. Statistical analyses were performed by two-tailed t-test/ t'-test or one-way analysis of variance (ANOVA) with Tukey post-hoc test. The numerical data were presented as mean  $\pm$  standard deviation. A value of  $p < 0.05$  was considered statistically significant ( $*p < 0.05$ ,  $**p < 0.01$ ,  $***p < 0.001$ ,  $****p < 0.0001$ ), and ns means no statistically significant difference.

### Reporting summary

Further information on research design is available in the Nature Portfolio Reporting Summary linked to this article.

### Data availability

The RNA sequencing data used in this study are available in the NCBI Sequence Read Archive (SRA) database under accession code: "PRJNA1004430". All other data supporting the findings of this study are available within the article and its supplementary files. Any additional requests for information can be directed to, and will be fulfilled by, the corresponding authors. Source data are provided in this paper. Source data are provided with this paper.

### Code availability

Analytical tools, variables, and sources of tutorials were described in the Methods section. R code is available from the corresponding author upon request.

### References

- Willyard, C. Unlocking the secrets of scar-free skin healing. *Nature* **563**, S86–s88 (2018).
- Boothby, I. C., Cohen, J. N. & Rosenblum, M. D. Regulatory T cells in skin injury: at the crossroads of tolerance and tissue repair. *Sci. Immunol.* **5**, eaaz9631 (2020).
- Shook, B. A. et al. Myofibroblast proliferation and heterogeneity are supported by macrophages during skin repair. *Sci. (N. Y., N. Y.)* **362**, eaar2971 (2018).
- Gay, D. et al. Phagocytosis of Wnt inhibitor SFRP4 by late wound macrophages drives chronic Wnt activity for fibrotic skin healing. *Sci. Adv.* **6**, eaay3704 (2020).
- Wang, X. et al. Macrophages induce AKT/ $\beta$ -catenin-dependent Lgr5(+) stem cell activation and hair follicle regeneration through TNF. *Nat. Commun.* **8**, 14091 (2017).
- Gay, D. et al. Fgf9 from dermal  $\gamma\delta$  T cells induces hair follicle neogenesis after wounding. *Nat. Med.* **19**, 916–923 (2013).
- Nelson, A. M. et al. Interleukin-6 null mice paradoxically display increased stat3 activity and wound-induced hair neogenesis. *J. Investigative Dermatol.* **136**, 1051–1053 (2016).
- Lee, P. et al. Stimulation of hair follicle stem cell proliferation through an IL-1 dependent activation of  $\gamma\delta$ T-cells. *eLife* **6**, e28875 (2017).
- Wynn, T. A. & Vannella, K. M. Macrophages in tissue repair, regeneration, and fibrosis. *Immunity* **44**, 450–462 (2016).
- Eming, S. A., Wynn, T. A. & Martin, P. Inflammation and metabolism in tissue repair and regeneration. *Sci. (N. Y., N. Y.)* **356**, 1026–1030 (2017).
- Murray, P. J. Macrophage polarization. *Annu. Rev. Physiol.* **79**, 541–566 (2017).
- Wang, G. et al. Bacteria induce skin regeneration via IL-1 $\beta$  signaling. *Cell host microbe* **29**, 777–791.e776 (2021).
- Xu, X. et al. The role of macrophages in the formation of hypertrophic scars and keloids. *Burns trauma* **8**, tkaa006 (2020).
- Knipper, J. A. et al. Interleukin-4 receptor  $\alpha$  signaling in myeloid cells controls collagen fibril assembly in skin repair. *Immunity* **43**, 803–816 (2015).
- Wier, E. et al. Neutrophil extracellular traps impair regeneration. *J. Cell. Mol. Med.* **25**, 10008–10019 (2021).
- Eberl, G. Immunity by equilibrium. *Nat. Rev. Immunol.* **16**, 524–532 (2016).
- Ali, N. & Rosenblum, M. D. Regulatory T cells in skin. *Immunology* **152**, 372–381 (2017).
- Henn, D. et al. Xenogeneic skin transplantation promotes angiogenesis and tissue regeneration through activated Trem2(+) macrophages. *Sci. Adv.* **7**, eabi4528 (2021).
- Kurita, M. et al. In vivo reprogramming of wound-resident cells generates skin epithelial tissue. *Nature* **561**, 243–247 (2018).
- Yi, B., Xu, Q. & Liu, W. An overview of substrate stiffness guided cellular response and its applications in tissue regeneration. *Bioact. Mater.* **15**, 82–102 (2022).

21. Sadtler, K. et al. Design, clinical translation and immunological response of biomaterials in regenerative medicine. *Nat. Rev. Mater.* **1**, 16040 (2016).
22. Hu, C. et al. Dissecting the microenvironment around biosynthetic scaffolds in murine skin wound healing. *Sci. Adv.* **7**, eabf0787 (2021).
23. Wang, C. et al. The diameter factor of aligned membranes facilitates wound healing by promoting epithelialization in an immune way. *Bioact. Mater.* **11**, 206–217 (2022).
24. Cui, T. et al. Large-scale fabrication of robust artificial skins from a biodegradable sealant-loaded nanofiber scaffold to skin tissue via microfluidic blow-spinning. *Adv. Mater. (Deerfield Beach, Fla.)* **32**, e2000982 (2020).
25. Yang, S. et al. MSC-derived sEV-loaded hyaluronan hydrogel promotes scarless skin healing by immunomodulation in a large skin wound model. *Biomed. Mater. (Bristol, England)* **17**, <https://doi.org/10.1088/1748-605X/ac68bc> (2022).
26. Shen, Y. et al. Sequential release of small extracellular vesicles from bilayered thiolated alginate/polyethylene glycol diacrylate hydrogels for scarless wound healing. *ACS nano* **15**, 6352–6368 (2021).
27. Zhang, Z. et al. Design of a biofluid-absorbing bioactive sandwich-structured Zn-Si bioceramic composite wound dressing for hair follicle regeneration and skin burn wound healing. *Bioact. Mater.* **6**, 1910–1920 (2021).
28. Ahmadian, Z. et al. A hydrogen-bonded extracellular matrix-mimicking bactericidal hydrogel with radical scavenging and hemostatic function for pH-responsive wound healing acceleration. *Adv. Healthc. Mater.* **10**, e2001122 (2021).
29. Sommerfeld, S. D. et al. Interleukin-36γ-producing macrophages drive IL-17-mediated fibrosis. *Sci. Immunol.* **4**, eaax4783 (2019).
30. Cherry, C. et al. Computational reconstruction of the signalling networks surrounding implanted biomaterials from single-cell transcriptomics. *Nat. Biomed. Eng.* **5**, 1228–1238 (2021).
31. Longo, S. K., Guo, M. G., Ji, A. L. & Khavari, P. A. Integrating single-cell and spatial transcriptomics to elucidate intercellular tissue dynamics. *Nat. Rev. Genet.* **22**, 627–644 (2021).
32. Ji, A. L. et al. Multimodal analysis of composition and spatial architecture in human squamous cell carcinoma. *Cell* **182**, 497–514.e422 (2020).
33. Berglund, E. et al. Spatial maps of prostate cancer transcriptomes reveal an unexplored landscape of heterogeneity. *Nat. Commun.* **9**, 2419 (2018).
34. Gao, S. et al. Identification of HSC/MPP expansion units in fetal liver by single-cell spatiotemporal transcriptomics. *Cell Res.* **32**, 38–53 (2022).
35. Foster, D. S. et al. Integrated spatial multiomics reveals fibroblast fate during tissue repair. *Proc. Natl Acad. Sci. USA* **118**, e2110025118 (2021).
36. Galiano, R. D., Michaels, J. T., Dobryansky, M., Levine, J. P. & Gurtner, G. C. Quantitative and reproducible murine model of excisional wound healing. *Wound Repair regeneration: Off. Publ. Wound Healing Soc. [J Eur. Tissue Repair Soc.]* **12**, 485–492 (2004).
37. Gounari, F. & Khazaie, K. TCF-1: a maverick in T cell development and function. *Nat. Immunol.* **23**, 671–678 (2022).
38. Zhao, X., Shan, Q. & Xue, H. H. TCF1 in T cell immunity: a broadened frontier. *Nat. Rev. Immunol.* **22**, 147–157 (2022).
39. Lau, C. I., Yáñez, D. C., Papaioannou, E., Ross, S. & Crompton, T. Sonic Hedgehog signalling in the regulation of barrier tissue homeostasis and inflammation. *FEBS J.* **289**, 8050–8061 (2022).
40. Ito, M. et al. Wnt-dependent de novo hair follicle regeneration in adult mouse skin after wounding. *Nature* **447**, 316–320 (2007).
41. Lim, C. H. et al. Hedgehog stimulates hair follicle neogenesis by creating inductive dermis during murine skin wound healing. *Nat. Commun.* **9**, 4903 (2018).
42. Kalekar, L. A. et al. Regulatory T cells in skin are uniquely poised to suppress profibrotic immune responses. *Sci. Immunol.* **4**, eaaw2910 (2019).
43. Driskell, R. R. et al. Distinct fibroblast lineages determine dermal architecture in skin development and repair. *Nature* **504**, 277–281 (2013).
44. Mok, K. et al. Dermal condensate niche fate specification occurs prior to formation and is placode progenitor dependent. *Developmental cell* **48**, 32–48.e35 (2019).
45. Liu, Y. et al. Hedgehog signaling reprograms hair follicle niche fibroblasts to a hyper-activated state. *Dev. Cell* **57**, 1758–1775.e1757 (2022).
46. Joost, S. et al. The molecular anatomy of mouse skin during hair growth and rest. *Cell Stem Cell* **26**, 441–457.e447 (2020).
47. Kim, D. et al. Noncoding dsRNA induces retinoic acid synthesis to stimulate hair follicle regeneration via TLR3. *Nat. Commun.* **10**, 2811 (2019).
48. Abbasi, S. et al. Distinct regulatory programs control the latent regenerative potential of dermal fibroblasts during wound healing. *Cell Stem Cell* **27**, 396–412.e396 (2020).
49. Guerrero-Juarez, C. F. et al. Single-cell analysis reveals fibroblast heterogeneity and myeloid-derived adipocyte progenitors in murine skin wounds. *Nat. Commun.* **10**, 650 (2019).
50. Buechler, M. B. et al. Cross-tissue organization of the fibroblast lineage. *Nature* **593**, 575–579 (2021).
51. Rinkevich, Y. et al. Skin fibrosis. Identification and isolation of a dermal lineage with intrinsic fibrogenic potential. *Sci. (N. Y., N. Y.)* **348**, aaa2151 (2015).
52. Lloyd, C. M. & Snelgrove, R. J. Type 2 immunity: Expanding our view. *Sci. Immunol.* **3**, eaat1604 (2018).
53. Telerman, S. B. et al. Dermal Blimp1 Acts Downstream of Epidermal TGFβ and Wnt/β-Catenin to Regulate Hair Follicle Formation and Growth. *J. Invest. Dermatol.* **137**, 2270–2281 (2017).
54. Ode Boni, B. O., Lamboni, L., Souho, T., Gauthier, M. & Yang, G. Immunomodulation and cellular response to biomaterials: the overriding role of neutrophils in healing. *Mater. Horiz.* **6**, 1122–1137 (2019).
55. Chu, C. et al. Modulation of foreign body reaction and macrophage phenotypes concerning microenvironment. *J. Biomed. Mater. Res. Part A* **108**, 127–135 (2020).
56. Mills, C. D., Kincaid, K., Alt, J. M., Heilman, M. J. & Hill, A. M. M-1/M-2 macrophages and the Th1/Th2 paradigm. *J. Immunol. (Baltim., Md.: 1950)* **164**, 6166–6173 (2000).
57. Yu, Y. et al. Single-cell RNA-seq identifies a PD-1(hi) ILC progenitor and defines its development pathway. *Nature* **539**, 102–106 (2016).
58. Bielecki, P. et al. Skin-resident innate lymphoid cells converge on a pathogenic effector state. *Nature* **592**, 128–132 (2021).
59. Whangbo, J. S. et al. Dose-escalated interleukin-2 therapy for refractory chronic graft-versus-host disease in adults and children. *Blood Adv.* **3**, 2550–2561 (2019).
60. Ali, N. et al. Regulatory T cells in skin facilitate epithelial stem cell differentiation. *Cell* **169**, 1119–1129.e1111 (2017).
61. Chang, D. T., Colton, E. & Anderson, J. M. Paracrine and juxtacrine lymphocyte enhancement of adherent macrophage and foreign body giant cell activation. *J. Biomed. Mater. Res. Part A* **89**, 490–498 (2009).
62. Bansal, R., van Baarlen, J., Storm, G. & Prakash, J. The interplay of the Notch signaling in hepatic stellate cells and macrophages determines the fate of liver fibrogenesis. *Sci. Rep.* **5**, 18272 (2015).
63. Sadtler, K. et al. Developing a pro-regenerative biomaterial scaffold microenvironment requires T helper 2 cells. *Sci. (N. Y., N. Y.)* **352**, 366–370 (2016).
64. Doloff, J. C. et al. Colony stimulating factor-1 receptor is a central component of the foreign body response to biomaterial implants in rodents and non-human primates. *Nat. Mater.* **16**, 671–680 (2017).

65. Monavarian, M., Kader, S., Moeinzadeh, S. & Jabbari, E. Regenerative scar-free skin wound healing. *Tissue Eng. Part B, Rev.* **25**, 294–311 (2019).
66. Mascharak, S. et al. Preventing engrailed-1 activation in fibroblasts yields wound regeneration without scarring. *Sci. (N. Y., N. Y.)* **372**, eaba2374 (2021).
67. Nosbaum, A. et al. Cutting edge: regulatory t cells facilitate cutaneous wound healing. *J. Immunol. (Baltim., Md.: 1950)* **196**, 2010–2014 (2016).
68. Feng, C. et al. Single-cell RNA sequencing reveals distinct immunology profiles in human keloid. *Front. Immunol.* **13**, 940645 (2022).

## Acknowledgements

The study was funded in part by the National Natural Science Foundation of China, grant 82271015 (Y.M.); Sichuan Science and Technology Program, grant 2022YFS0041 (Y.Q.) & 2022ZYD0052 (Y.M.); Interdisciplinary Innovation Project, West China Hospital of Stomatology, Sichuan University, grant RD-03-202006 (Y.M.). We thank the Novogene company for RNA sequencing work and Yukai Wang for the assistance of bioinformatics analysis, the National Clinical Research Center for Oral Diseases & State Key Laboratory of Oral Diseases for animal experiments, and the Analytical & Testing Center of Sichuan University for the fabrication of biomaterials. We thank Xinhui Li, Jiayu Gao for the help with analysis.

## Author contributions

Y.Y., C.C., Y.M. and Y.Q. conceived the project. Y.Y. designed and performed all the experiments with the assistance of C.C., L.L., C.W. and C.H. Data were analyzed by Y.Y. and S.R. with the help of C.H. The manuscript was written by Y.Y. with the guidance of C.C. and Y.M. The project was supervised by Y.M. and Y.Q. jointly.

## Competing interests

The authors declare no competing interests.

## Additional information

**Supplementary information** The online version contains supplementary material available at <https://doi.org/10.1038/s41467-023-41608-9>.

**Correspondence** and requests for materials should be addressed to Yi Man or Yili Qu.

**Peer review information** *Nature Communications* thanks the anonymous reviewers for their contribution to the peer review of this work. A peer review file is available.

**Reprints and permissions information** is available at <http://www.nature.com/reprints>

**Publisher's note** Springer Nature remains neutral with regard to jurisdictional claims in published maps and institutional affiliations.

**Open Access** This article is licensed under a Creative Commons Attribution 4.0 International License, which permits use, sharing, adaptation, distribution and reproduction in any medium or format, as long as you give appropriate credit to the original author(s) and the source, provide a link to the Creative Commons license, and indicate if changes were made. The images or other third party material in this article are included in the article's Creative Commons license, unless indicated otherwise in a credit line to the material. If material is not included in the article's Creative Commons license and your intended use is not permitted by statutory regulation or exceeds the permitted use, you will need to obtain permission directly from the copyright holder. To view a copy of this license, visit <http://creativecommons.org/licenses/by/4.0/>.

© The Author(s) 2023, corrected publication 2023